

Dzyalonshinskii-Moriya interaction in Fe_5GeTe_2 epitaxial thin films

J. Sampaio,^{*,†} A. Pascaud,[†] E. Quero,[†] A. Thiaville,[†] V. Polewczyk,[‡] A. Marty,[‡]
F. Bonell,[‡] and A. Mougin[†]

[†] *Université Paris-Saclay, CNRS, Laboratoire de Physique des Solides, 91405 Orsay, France*

[‡] *University Grenoble Alpes, CNRS, CEA, IRIG-Spintec, Grenoble, France*

E-mail: joao.sampaio@cnr.fr

March 25, 2025

Abstract

Van der Waals ferromagnets, such as Fe_5GeTe_2 , offer a promising platform for spintronic devices based on chiral magnetic textures, provided a significant Dzyaloshinskii-Moriya interaction (DMI) can be induced to stabilise them. Here, we directly measure DMI in epitaxial Fe_5GeTe_2 thin films using Brillouin light scattering spectroscopy and observe a consistent DMI ($D = 0.04 \text{ mJ/m}^2$) across various thicknesses. Its weak thickness dependence, combined with the nominally symmetric film interfaces, suggests a bulk origin. Although we do not determine the microscopic mechanism, our findings are compatible with ab-initio calculations linking DMI to partial ordering of Fe split sites. Additionally, we find a low magnetic dissipation ($\alpha < 0.003$). The observed DMI, which could be further enhanced by optimising the Fe site ordering, combined with low dissipation, makes Fe_5GeTe_2 a strong candidate for exploring the dynamics of chiral magnetic textures in two-dimensional materials.

Keywords

van der Waals magnets, Dzyaloshinskii-Moriya Interaction, Chiral spin textures, Fe_5GeTe_2

Introduction

Ferromagnetic van der Waals (vdW) materials present an interesting new class of materials for the study of nanomagnetism. Their structure, made of 2D layers with relatively weak inter-layer bonding, can produce very thin films with flat and clean surfaces, either by exfoliation from macroscopic crystals or epitaxial growth. This structure also lends itself naturally to the fabrication of heterostructures with good interfacial quality with a large variety of other vdW materials (semiconductors, metals, insulators, topological insulators, ...) — ideal for studying interfacial magnetic effects that are the basis of spintronic devices. Among the growing list of vdW ferromagnets of interest to spintronics, the Fe_xGeTe_2 family stands out due to their high Curie temperature,¹ metallic character, and large magneto-transport effects.

Moreover, there have been reports of chiral magnetic structures in Fe_xGeTe_2 , opening the way to their use in the many proposed devices based on chiral textures such as skyrmions. Homochiral spin spirals were observed in exfoliated flakes of Fe_3GeTe_2 ² (thickness $t = 185 \text{ nm}$), and Néel skyrmions were reported in Fe_3GeTe_2 (70 nm)/[Co/Pd]³ and $\text{WTe}_2/\text{Fe}_3\text{GeTe}_2$ (32 nm)⁴ heterostructures. In other members of the Fe_xGeTe_2 family, Néel skyrmions were observed in $\text{Fe}_{5-x}\text{GeTe}_2$ ^{5,6} (on 61 and 100 nm thick flakes), as well as in $(\text{FeCo})_5\text{GeTe}_2$ (110 nm).⁷ On the other hand, other groups working also on flakes of Fe_5GeTe_2 observed only non-chiral Bloch bub-

bles.^{8,9}

The observation of homo-chiral textures suggests a significant Dzyaloshinskii-Moriya interaction (DMI). Indeed, a large DMI parameter ($D = 1.0 \text{ mJ/m}^2$) was estimated in ref.⁴ A nonzero DMI requires a symmetry-breaking mechanism along the out-of-plane direction. However, both Fe_3GeTe_2 and Fe_5GeTe_2 are presumed to have inversion-symmetric crystal structures incompatible with DMI.¹⁰ Nevertheless, several experimental studies suggest that the actual crystalline structure of Fe_xGeTe_2 may lack inversion symmetry. Possible sources of symmetry breaking include Fe split-site ordering,¹¹ Fe self-intercalation in the van der Waals gaps,¹² ordered Te vacancies,⁹ and asymmetric Fe vacancy distribution.¹³ Additionally, deviations from the expected vdW stacking sequence (ABCABC in Fe_5GeTe_2 and ABAB in Fe_3GeTe_2) could also break inversion symmetry.

Additionally, large DMI has been observed in ultra-thin magnets with a symmetric bulk structure, such as nanometric Co films in a $\text{AlO}_x/\text{Co}/\text{Pt}$ triplet film (up to $D = 2 \text{ mJ/m}^2$ ¹⁴). In these cases, the DMI does not arise from the bulk crystalline structure but instead from asymmetric interfaces of the ultra-thin magnetic layer, which can be engineered to increase the effect. Although this interfacial mechanism could be expected to be weaker in vdW materials due to their weak interlayer coupling, first-principle calculations by Park et al.¹⁵ show that the interface of Fe_3GeTe_2 with its natural oxide can induce a significant DMI ($\approx 2 \text{ mJ/m}^2$ for a monolayer of Fe_3GeTe_2). Interfacial mechanisms, however, are only significant in ultra-thin systems and all the cited experimental observations were done in relatively thick (30 to 200 nm) exfoliated flakes.

Characterizing the DMI solely from the observation of magnetic textures is challenging, as these are influenced by multiple interactions, including dipolar effects, magnetocrystalline anisotropy, and exchange. In some cases, dipolar interactions may even create seemingly chiral textures at the surface of thick samples.^{3,16} To determine the origin of chiral magnetic textures and disentangle interfacial and bulk contributions, a more direct measurement of the DMI is essential. In this letter, we investigate the static and dynamic magnetic properties of epitaxial Fe_5GeTe_2 thin films of varying

thickness using Brillouin light scattering (BLS) spectroscopy. By directly measuring the DMI, we unambiguously demonstrate the presence of a significant DMI of bulk origin. Furthermore, we show that the magnetic damping in these films is low compared to conventional metallic ferromagnets. These properties make Fe_5GeTe_2 a promising material for the study of the propagation of chiral magnetic textures.

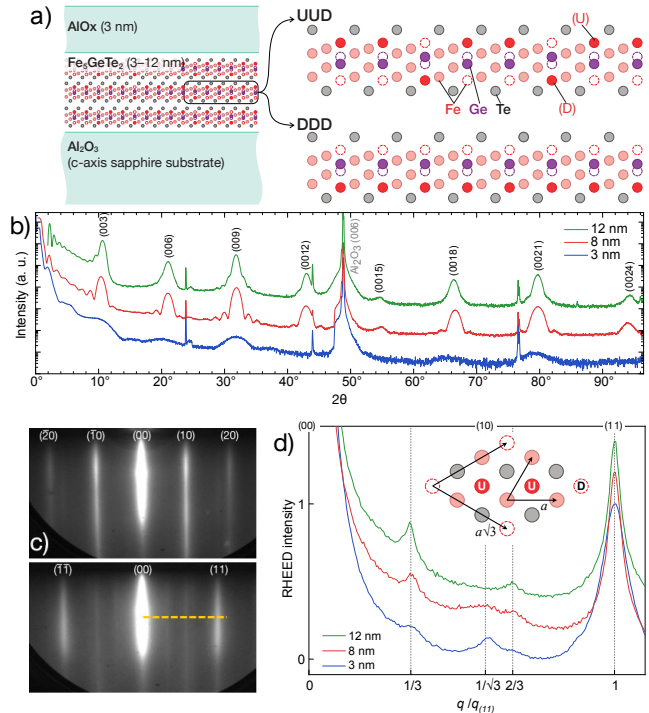


Figure 1: a) Sample structure and diagrams of ordered split sites Fe_5GeTe_2 with broken centrosymmetry: full ordering (“DDD”) or 1/3 (“UUD”). Open circles represent empty sites. b) XRD spectrum for the three films. c) RHEED along the (100) and (110) reciprocal directions, obtained after growth (3-nm thick film). d) RHEED intensity profiles along the dashed line in c. The profiles are normalized to the (11) intensity and shifted vertically for clarity. Inset: Top view schematic of the “UUD” $\sqrt{3} \times \sqrt{3}$ reconstruction.

Results

Sample growth & structure

Fe_5GeTe_2 films ($t = 12, 8$ and 3 nm) were epitaxially grown on $\text{Al}_2\text{O}_3(0001)$. The 12-nm-thick

film studied here was characterised in depth by Ribeiro et al.,¹⁷ and all films were grown following the protocol reported in that work. The films were capped by 3 nm of Al deposited at room temperature, then naturally oxidized in air. This capping layer prevents the oxidation of Fe₅GeTe₂ and provides symmetric top and bottom interfaces (Fig. 1a). The good crystalline quality of the 12-nm film was observed by X-ray diffraction (XRD) and scanning transmission electron microscopy.¹⁷ In line with this result, the XRD scans in Fig. 1b demonstrate a well-defined Fe₅GeTe₂ lattice for all layers. From these XRD measurements, the thickness of one Fe₅GeTe₂ monolayer is found equal to 0.98 nm, independently of the film thickness. The RHEED patterns of Fe₅GeTe₂ (8 nm) in the (100) and (110) reciprocal directions, measured after growth, are shown in Fig. 1c. Similar anisotropic diffraction patterns are observed at all thicknesses and demonstrate the good epitaxy on sapphire. However, faint (10) diffraction rods are visible in the (110) direction (peak at $q/q(11) = 1/\sqrt{3}$ in Fig. 1d). They denote the presence of a small proportion of domains that are rotated by 30° from the main crystal orientation. This feature is more apparent for the thinnest layer and disappears for the 12 nm film, indicating an improvement of the crystal in-plane orientation quality with increasing thickness. In addition, the RHEED patterns display a (3×1) reconstruction characteristic of a $(\sqrt{3} \times \sqrt{3}) R30^\circ$ superstructure (peaks at $q/q(11) = 1/3$ and $2/3$ in Fig. 1d). This superstructure is observed in all three films, and is more apparent at larger thicknesses.

Fe₅GeTe₂ is expected to have two partially-filled Fe sites (“split sites”) at different vertical positions in the elementary monolayer, “U” or “D” (see Fig. 1a). The $\sqrt{3} \times \sqrt{3}$ superstructure may be attributed to a large-scale lateral ordering of the Fe split sites in a “UUD” or “UDD” pattern (inset of Fig. 1d), which was previously experimentally observed by Ly et al.¹¹ and found to be more energetically stable than the “UUU” ordering by *ab initio* calculations.¹⁸ This superstructure is also compatible with an ordering of Te vacancies as reported by Gopi et al.⁹ Both these structures break the inversion symmetry of the crystal. The presence of this superstructure in the deeper layers of the films (beyond their top surface) cannot be as-

sessed from these RHEED measurements, which were recorded after the deposition.

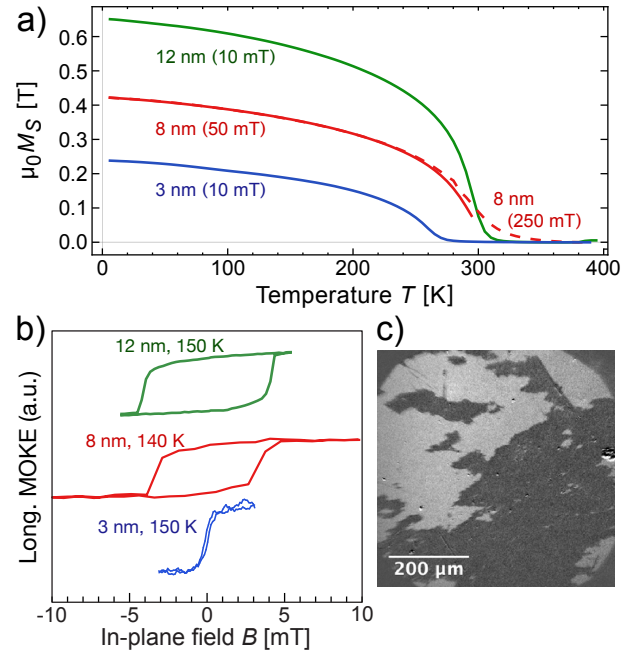


Figure 2: a) $M_s(T)$ of the three films under in-plane field (SQUID measurement). b) LMOKE hysteresis loops of the three films close to 150 K. c) In-plane magnetic domains in the 12-nm-thick sample imaged by LMOKE (the contrast orientation is left/right).

Magnetic properties

The spontaneous magnetization (M_s) of the three samples was measured by SQUID magnetometry as a function of temperature (Fig. 2). Thinner films showed lower M_s , with the 3-nm film showing about one-third of the M_s of the 12-nm film at 150 K (see Table 1). The Curie temperature (T_C) of the thicker films (297–299 K) is similar to bulk values (270–310 K¹⁹), whereas the 3-nm film had a lower T_C (258 K). The evolution of M_s and T_C indicates that a thickness of a few layers is needed to fully develop the bulk magnetic properties of the films. The $M_s(T)$ curves showed a monotonic trend, unlike previous reports of transitions in $M_s(T)$.^{1,8,11,20} However, those studies focused on virgin films, whereas our samples had been previously magnetized. These transitions may also be specific to bulk samples rather than epitaxially-grown films.

Hysteresis loops measured at 150 K by longitudinal magneto-optical Kerr effect (LMOKE) (Fig. 2b) show in-plane magnetization reversal with a small coercive field of a few mT around 150 K. The sharp transitions in the loops indicate reversal by nucleation and domain wall propagation, typical of homogeneous films. LMOKE imaging of the 12-nm film (Fig. 2c) confirms domain wall propagation during reversal and reveals large domains (10–100 μm), further indicating film homogeneity.

The samples were further characterised by studying the spin wave frequency as a function of field and wave vector using BLS spectroscopy (see Methods). The negative anisotropy field B_K extracted from the BLS measurements of frequency versus field confirms the easy-plane anisotropy (at 150 K; Tab. 1). Its magnitude is significantly larger than the expected contribution from shape anisotropy (given by $-\mu_0 M_s$), a behavior previously observed in Fe_5GeTe_2 .^{1,17} This suggests either the presence of an intrinsic easy-plane magnetocrystalline anisotropy or that the magnetisation is inhomogeneous across the vdW layers and gaps, leading to a stronger shape anisotropy than expected from the measured M_s .¹

The g-factor obtained from the BLS measurements (see Methods) consistently falls in the range $g = 2.1 - 2.3$, showing no significant temperature dependence, in close agreement with previous reports.^{1,21} The notable deviation from the free-electron value of $g = 2.0$ suggests a substantial orbital moment and significant spin-orbit coupling in the material. This is consistent with the orbital/spin moment ratio measured in.¹⁷

¹Assuming a homogeneous M_s when it actually varies along the film thickness, $M_s(z)$, results in an underestimation of the shape anisotropy K_d . K_d is the difference of dipolar energy density between the in-plane and perpendicular magnetisation states. The average dipolar energy density is $-\langle \frac{\mu_0}{2} \mathbf{H}_d(z) \cdot \mathbf{M}(z) \rangle$, where $\mathbf{H}_d(z)$ is the local dipolar field and $\langle \dots \rangle$ denotes an average along the thickness ($\frac{1}{t} \int_0^t \dots dz$). In the in-plane state, $\mathbf{H}_d = 0$, while in the perpendicular state $\mathbf{H}_d(z) = -M_s(z)\hat{\mathbf{z}}$. This leads to

$$K_d = -\frac{\mu_0}{2} \langle M_s^2(z) \rangle.$$

Since it is always the case that $\langle M_s^2(z) \rangle \geq \langle M_s(z) \rangle^2$, K_d is always larger than the value calculated using the average magnetisation: $|K_d| \geq \frac{\mu_0}{2} \langle M_s(z) \rangle^2$ (where $\langle M_s(z) \rangle$ is the magnetisation given by macroscopic magnetometry measurements)

The Gilbert dissipation parameter (α) can be inferred from the BLS peak width (Γ), similar to its extraction from ferromagnetic resonance measurements. However, Γ is also broadened by inhomogeneities in the film's magnetic properties, which are typically separated using high magnetic fields due to their distinct field dependence. Since the available field was insufficient for this separation, we estimated an upper bound, α_{eff} (see Fig. 5 and Methods). The lowest α_{eff} values for each film are listed in Table 1. The α_{eff} is larger for thinner films, which could be due to a higher dissipation, as is often observed in other magnetic films (e.g.²²). It may also be due to a higher inhomogeneity of the magnetic properties, as the properties of thinner films are more affected by variations of the thickness or of the interfaces. Overall, α_{eff} as low as $3 \cdot 10^{-3}$ were observed, which is lower than most typical metals ($\sim 10^{-2}$) and lower than reported measurements in bulk Fe_5GeTe_2 .¹ A low magnetic dissipation parameter enables the motion of textures with lower applied torques, such as skyrmions driven by spin currents, adding to the interest of Fe_5GeTe_2 as a material to study chiral textures.

DMI

The Stokes and anti-Stokes peaks in the BLS spectrum (Fig. 3a) correspond to cycloidal spinwaves of opposite rotation sense (Fig. 3b), and are subject to an opposite energy contributions from the DMI. In the limit of thin films ($kt \ll 1$, where k is the wave vector of the spinwave determined by the incidence angle of the light), as is the case here, the difference in frequency between the Stokes and anti-Stokes peaks ($\Delta f \equiv |f_{\text{anti-Stokes}}| - |f_{\text{Stokes}}|$) can be fully attributed to this effect, and can be used to determine the DMI parameter D :^{14,23}

$$\Delta f = \frac{2\gamma}{M_s} Dk, \quad (1)$$

where $\gamma = g\mu_B/\hbar$ is the gyromagnetic ratio (and μ_B and \hbar are the Bohr's magneton and the reduced Planck constant, respectively.) As there may be a small constant Δf due to an imperfect alignment of the spectrometer, several spectra were measured and the slope of $\Delta f(k)$ (which we dub v_{DMI}) was

Table 1: Material parameters at 150 K for the three films. The T_C and $\mu_0 M_s$ were determined from SQUID magnetometry, B_K and the gyromagnetic g -factor were taken from fits of the BLS frequency versus field curves, the α (an upper bound; see text) from the peak width, and v_{DMI} from fits of the Stokes/anti-Stokes frequency difference. The negative B_K represents an easy-plane anisotropy.

t nm	T_C K	$\mu_0 M_s$ T	B_K T	g	α	v_{DMI} m/s	D $\mu\text{J}/\text{m}^2$
3	258	0.19	-0.59	2.3	< 0.03	18 ± 4	22 ± 5
8	299	0.36	-0.84	2.2	< 0.005	20.5 ± 1.5	47 ± 3
12	297	0.57	-1.0	2.1	< 0.003	10.9 ± 1.3	41 ± 5

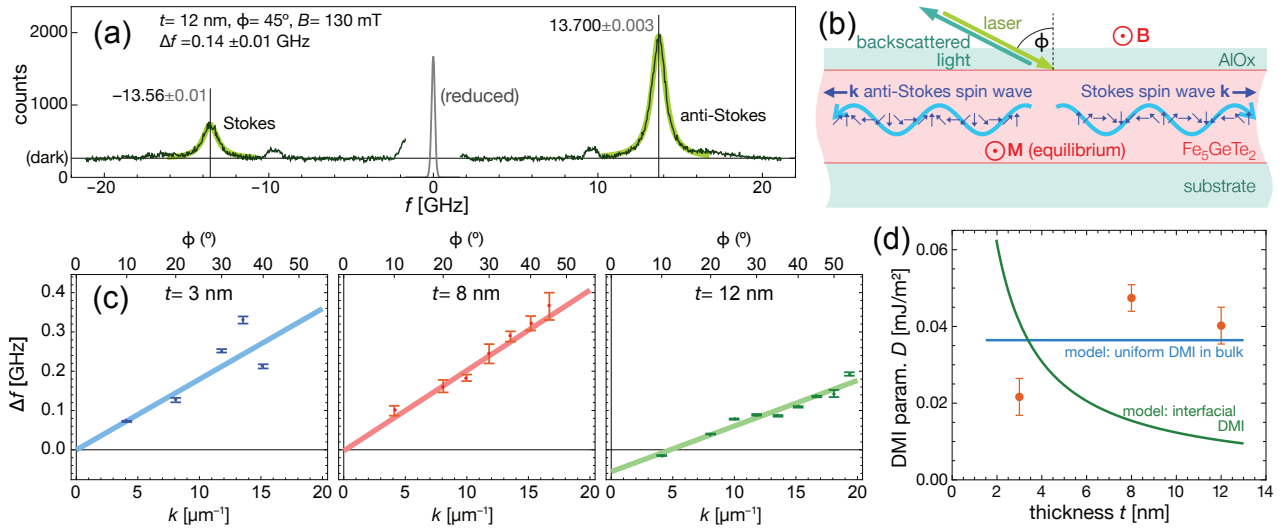


Figure 3: a) Example of a BLS spectrum of the 12 nm film, in black, taken at $\phi = 45^\circ$ (150 K, $B = 130$ mT). The green lines show the fit to a Lorentzian peak (with the fitted centres written above the peaks). The central peak corresponds to non-scattered light and shows the instrumental width. b) Schematic of the BLS geometry. c) Stokes/anti-Stokes frequency difference, Δf , versus wave vector k for the three films (points; taken at $B = 211$, 250, and 130 mT, respectively.) The linear fits (lines) are used to extract v_{DMI} and D . The offset of the fit accounts for a possible imperfect alignment of the spectrometer. d) Extracted D versus sample thickness t (points) and fits assuming a uniform bulk origin (constant blue line) and an interfacial origin ($\propto 1/t$, green line).

determined. The expected reversal of the sign of Δf with a reversal of the field direction was also verified. Fig. 3c shows the measured $\Delta f(k)$ for the 3, 8 and 12 nm films at 150 K. We observe that there is clearly a linear slope and thus a finite D in all three films. All three show a slope, and thus a DMI, of the same sign. With the geometry of our setup ($\mathbf{k}_{\text{Stokes}} \times \mathbf{B}$ pointing into the film surface, Fig. 3b), this positive slope corresponds to favoured right-handed spinwaves, and thus a positive DMI parameter. The calculated D parameters (using eq. 1) are shown in Tab. 1 for the three films.

As a verification, the DMI was also measured in one of the films ($t = 8$ nm) at room temperature, and no DMI was observed, as expected when approaching T_C .

The measured DMI varies between $D = 0.02$ to 0.05 mJ/m² and is comparable to the values typically observed in spintronic systems, although lower than the highest known effects (for reference, the strong interfacial DMI in Co/Pt would yield approximately 0.2 mJ/m² in a 8-nm-thick film¹⁴).

Discussion

The observation of DMI requires broken inversion symmetry along the c -axis, either in the bulk of the material or due to asymmetric interfaces. This symmetry breaking must persist over a large lateral scale, as BLS measurements average over the 30- μm laser spot and are consistent between points several 10s of μm apart. The dependence of D on film thickness t can help distinguish between bulk and interfacial origins: a bulk contribution would result in a constant D , whereas an interfacial contribution should scale as $D \propto 1/t$.¹⁴ Figure 3d shows $D(t)$ along with best-fit curves for both scenarios. Clearly, the data do not follow the $1/t$ trend expected for interfacial DMI. This finding aligns with the rather symmetric environment of our films, which have two electronically similar interfaces ($\text{Al}_2\text{O}_3/\text{Fe}_5\text{GeTe}_2$ and $\text{Fe}_5\text{GeTe}_2/\text{AlO}_x$). Instead, the $D(t)$ data is more compatible with the constant behaviour of a bulk origin, with a $D = 0.04$ to 0.05 mJ/m², as measured in the thickest films. The weaker DMI in the 3-nm-thick film, which correlates with lower M_s and T_C , can be at-

tributed to weaker ferromagnetism in the ultrathin regime.

Given these observations, the symmetry-breaking mechanism responsible for the DMI must extend throughout the film thickness, up to 12 nm. We now discuss three possible mechanisms. The ideal structure of Fe_5GeTe_2 is a rhombohedral stacking of centrosymmetric monolayers in the nonpolar ABCABC sequence (space group $R\bar{3}m$). Disruptions to this sequence by stacking faults could locally break inversion symmetry.²⁴ Indeed, cross-sectional transmission electron microscopy images reveal a high density of stacking faults in our films,¹⁷ consistent with observations in bulk crystals that were slowly cooled to room temperature after growth.²⁵ However, we did not identify any specific stacking sequence that would lead to a net nonzero DMI across the film thickness or a consistent DMI sign across different samples.

A second mechanism involves symmetry breaking within the Fe_5GeTe_2 vdW layers. This is supported by our RHEED observations of a $\sqrt{3} \times \sqrt{3}$ superstructure, which cannot derive from a specific vdW stacking. A non-centrosymmetric phase with a $\sqrt{3} \times \sqrt{3}$ superstructure was reported by Gopi et al.,⁹ who ascribed it to a pattern of 1/3 Te vacancies ordered along the perpendicular direction. Since this phase represented only a small fraction ($< 10^{-2}$) of the studied bulk crystals, it was deemed to have a negligible effect on the material's DMI. While this phase might be more prevalent in epitaxial films, Rutherford backscattering analysis of our films¹⁷ showed no significant Te depletion, suggesting that this mechanism is unlikely to explain our results².

Other groups interpreted this $\sqrt{3} \times \sqrt{3}$ superstructure as the ordering of Fe split sites (“D” and “U” sites in Fig. 1a,d).^{11,19} In the centrosymmetric structure, these sites are equally and randomly populated. However, *ab initio* calculations showed that the “UDD” and “UUD” configurations are energetically more favorable.¹⁸ While our RHEED measurements cannot determine whether this ordering extends beyond the top layer, electron microscopy analyses in Ref.¹⁹ showed a simi-

²The Te stoichiometry in the 12-nm film was measured to be $\text{Te}_{2\pm 0.08}$.¹⁷ A full pattern of 1/3 Te vacancies in one of the sides of all vdW layers (i.e., a loss of 1/6 of the expected Te) would give $\text{Te}_{1.7}$.

lar short-range order in the bulk of Fe_5GeTe_2 . Three groups have calculated the DMI assuming a perfectly ordered “UUU” arrangement in a monolayer, using different computational methods.^{5,26,27} Their predicted $|D|$ values vary significantly (0.76, 0.6, and 0.06 mJ/m^2), despite all employing commonly used techniques. Our measured $|D|$ (0.04 – 0.05 mJ/m^2) is comparable to the lowest theoretical estimate, and much lower than the highest prediction. This quantitative difference may be due to several reasons. First, the calculations do not account for temperature, which reduces the macroscopic D . Second, our films are not ordered in the “UUU” configuration since this would be inconsistent with the observed $\sqrt{3} \times \sqrt{3}$ superstructure. According to Ghosh et al.,²⁷ the DMI of the “UUD” or “UDD” configurations is only slightly lower than that of the “UUU” configuration ($|D| = 0.05$ instead of 0.06 mJ/m^2), contrary to the naïve expectation of a 2/3 reduction. Finally, by symmetry, the “UUD” and “UDD” configurations contribute equally but with opposite sign DMI. While one of the two must be dominant to account for the observed DMI, the other may be present in a smaller amount and partially compensate the net DMI.

Assuming that the DMI arises from an ordering of the Fe split sites, the sign of D can be used to infer the dominant split-site configuration. Both refs.²⁶ and⁵ found that a fully-ordered “UUU” configuration favours counter-clockwise spinwaves, corresponding to a negative DMI. Therefore, the observed positive DMI suggests that the predominant ordering in our films is “UDD.”

The presence of a symmetry-breaking mechanism extending both laterally over large scales and through the film thickness, combined with the consistent DMI sign observed in all three films, indicates a robust and reproducible effect. This suggests that the symmetry breaking is likely associated with the growth process, which is inherently asymmetric.

Conclusion

In conclusion, we have used BLS to quantitatively measure a significant DMI in several epitax-

ial Fe_5GeTe_2 films with nominally symmetric interfaces. The DMI values were consistent across films of different thicknesses and exhibited the same sign, indicating a bulk origin for the DMI. Although our measurements cannot reveal the microscopic origin of the DMI, they are consistent with a partial ordering of the Fe split sites during film growth, a mechanism supported by published *ab initio* calculations showing that such ordering induces DMI.

These results confirm that Fe_5GeTe_2 can host a significant DMI and suggest that the reported magnetic textures in Fe_5GeTe_2 are likely chiral in nature. If the mechanism for the non-centrosymmetric structure is indeed induced during the growth as we suggest, the DMI may be enhanced by adjusting the growth conditions. Additionally, DMI might be stronger in Fe_5GeTe_2 films synthesized or processed using other techniques.

The bulk DMI mechanism observed here may coexist with interfacial contributions, such as those involving oxide layers as considered in previous studies, offering opportunities to further enhance the DMI.

With its significant bulk DMI, low magnetic dissipation, and the potential to engineer its interfaces, Fe_5GeTe_2 emerges as a promising material for exploring the dynamics of chiral magnetic textures and enabling spintronic applications.

Methods

Determination of magnetic parameters from BLS spectroscopy

BLS spectroscopy was used to analyse the spin-wave frequency as a function of field or wavevector. A green laser beam ($\lambda = 532$ nm) was directed onto the sample at an angle ϕ (Fig. 3b), with the sample placed inside a cryostat at a controlled temperature. A magnetic field was applied using permanent magnets to align the equilibrium magnetization in the film plane and perpendicular to the incident light, following the Damon-Eshbach geometry. The backscattered light was analysed with a double, three-pass Fabry-Perot spectrometer (model TFP2-HC from JRS Instruments). Some of the light is backscattered by spin-

waves, with a wave vector defined by the incidence angle as $k = 4\pi \sin \phi / \lambda$. This produces two peaks in the spectrum: a redshifted (Stokes) peak corresponding to forward-propagating spin waves, and a blueshifted (anti-Stokes) peak corresponding to back-propagating spin waves. The incident and analysed light are cross-polarised, which suppresses most peaks arising from phonon scattering. The observed peaks were characterized by their average frequency (f_0), their frequency difference (Δf), and their full width at half maximum (Γ), all obtained by fitting the peaks with a Lorentzian profile. The variation of these frequencies as a function of field or wavevector can be used to determine static (D , B_K , M_s , ...) and dynamic parameters (g and α).

The effective anisotropy field B_K and g-factor g are extracted from the variation with field of the mean frequency of the Stokes and anti-Stokes peak, f_0 , by using the law of dispersion of magnetostatic spinwaves determined by Kalinikos & Slavin:^{14,28}

$$f_0 = \frac{\gamma}{2\pi} \sqrt{B + \mu_0 M_s P + \frac{2A}{M_s} k^2} \sqrt{(B - B_K) - \mu_0 M_s P + \frac{2A}{M_s} k^2} \quad (2)$$

where $P \approx kt/2$ for thin films ($kt \ll 1$) and A is the exchange stiffness (which is neglected in our analysis).

Fig. 4a shows BLS spectra of the 8-nm sample taken at different applied fields B . All spectra clearly show the Stokes and anti-Stokes peaks, which are of different amplitude, typical of magnon BLS (but not of phonons). The mean frequency f_0 is shown versus B in Fig. 4b, and is fitted using eq. 2 (lines in the plot.) The determined B_K and g parameters using this method are shown in Tab. 1 for all three films at 150 K.

Determination of the Gilbert dissipation parameter

Some information on the Gilbert dissipation parameter α can be obtained from the peak width Γ . The main contributions to Γ are the instrumental resolution (Γ_0), the magnetic dissipation, and the inhomogeneity of the magnetic properties such as

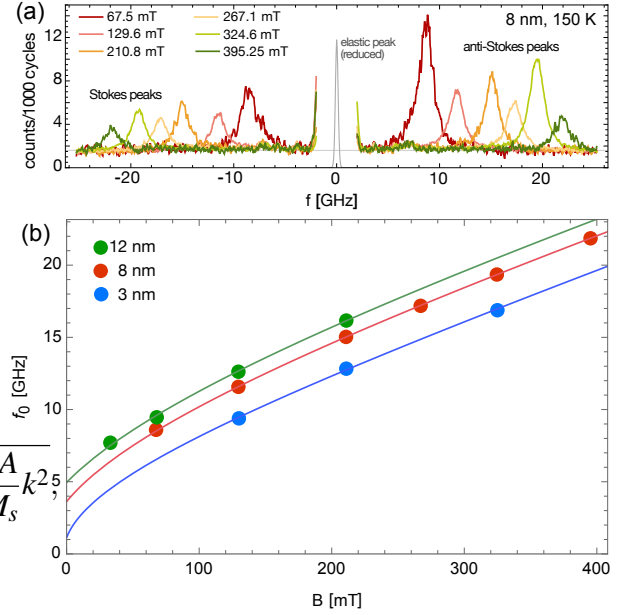


Figure 4: a) BLS spectra of the 8 nm film, at different applied fields (150 K, $\phi = 30^\circ$). The central peak corresponds to unscattered light and is used to evaluate the instrumental linewidth. b) Spin-wave frequency versus applied field for the three film thicknesses (150 K) ($\phi = 20^\circ$ for the 3 and 12 nm films, 30° for the 8 nm). The lines are fits using the model of Kalinikos and Slavin,²⁸ neglecting the contribution of the exchange interaction.

the anisotropy (δB):

$$\Gamma = \Gamma_0 + \gamma\alpha(2B - B_K) + \gamma\delta B F(B, B_K), \quad (3)$$

where $F()$ is a function that tends towards a constant for $B \gg B_K$ (see SI of ref.²⁹). The measured Γ vs. B is shown in Fig. 5 for the three films.

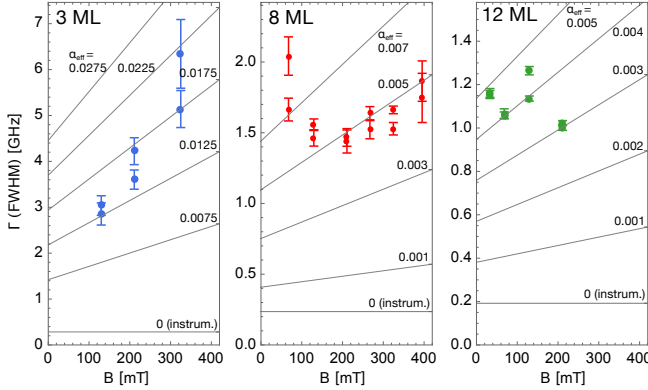


Figure 5: Peak FWHM Γ versus field B for the three films. The grey lines are the expected variation assuming different values of α_{eff} (see text for details on the calculation of α_{eff}).

The instrumental width Γ_0 is measured from the elastic peak at $f = 0$ (seen in Fig. 4a). The inhomogeneity contribution δB may be disentangled from the dissipation by applying a large field such that $\alpha(2B - B_K) \gg \delta B F(B, B_K)$, however this was not possible with our setup. An upper bound of the dissipation parameter, α_{eff} , can be determined by neglecting the contribution from inhomogeneity:

$$\alpha_{\text{eff}} = (\Gamma - \Gamma_0)/(\gamma(2B - B_K)) \geq \alpha \quad (4)$$

The calculated α_{eff} is shown as grey lines in fig. 5.

Acknowledgement The authors thank V. Jedy for his support with cryogenic measurements. Magnetometry measurements were kindly performed by E. Rivière at ICMMO (CNRS) and also at the Physical Measurements Platform at the LPS. This work was supported by the French National Research Agency (ANR) through the projects ELMAX (ANR-20-CE24-0015), NEXT (ANR-23-CE09-0034), the FLAG-ERA grant MNEMOSYN (ANR-21-GRF1-0005-01), and the LANEF framework for mutualized infrastructure (ANR-10-LABX-51-01).

References

- (1) Alahmed, L. et al. Magnetism and spin dynamics in room-temperature van der Waals magnet Fe₅GeTe₂. *2D Materials* **2021**, *8*, 045030.
- (2) Meijer, M. J.; Lucassen, J.; Duine, R. A.; Swagten, H. J.; Koopmans, B.; Lavrijsen, R.; Guimarães, M. H. D. Chiral Spin Spirals at the Surface of the van der Waals Ferromagnet Fe₃GeTe₂. *Nano Letters* **2020**, *20*, 8563–8568.
- (3) Yang, M. et al. Creation of skyrmions in van der Waals ferromagnet Fe₃GeTe₂ on (Co/Pd)_n superlattice. *Science Advances* **2020**, *6*.
- (4) Wu, Y. et al. Néel-type skyrmion in WTe₂/Fe₃GeTe₂ van der Waals heterostructure. *Nature Communications* **2020**, *11*.
- (5) Gao, Y.; Yan, S.; Yin, Q.; Huang, H.; Li, Z.; Zhu, Z.; Cai, J.; Shen, B.; Lei, H.; Zhang, Y.; Wang, S. Manipulation of topological spin configuration via tailoring thickness in van der Waals ferromagnetic Fe_{5-x}GeTe₂. *Physical Review B* **2022**, *105*, 014426.
- (6) Casas, B. W.; Li, Y.; Moon, A.; Xin, Y.; McKeever, C.; Macy, J.; Petford-Long, A. K.; Phatak, C. M.; Santos, E. J. G.; Choi, E. S.; Balicas, L. Coexistence of Merons with Skyrmions in the Centrosymmetric Van Der Waals Ferromagnet Fe_{5-x}GeTe₂. *Advanced Materials* **2023**, *35*.
- (7) Zhang, H. et al. Room-temperature skyrmion lattice in a layered magnet (Fe_{0.5}Co_{0.5})₅GeTe₂. *Science Advances* **2022**, *8*.
- (8) Schmitt, M.; Denneulin, T.; Kovács, A.; Saunderson, T. G.; Rübmann, P.; Shahee, A.; Scholz, T.; Tavabi, A. H.; Gradhand, M.; Mavropoulos, P.; Lotsch, B. V.; Dunin-Borkowski, R. E.; Mokrousov, Y.; Blügel, S.; Kläui, M. Skyrmionic spin structures in layered Fe₅GeTe₂ up to room temperature. *Communications Physics* **2022**, *5*.

- (9) Gopi, A. K.; Srivastava, A. K.; Sharma, A. K.; Chakraborty, A.; Das, S.; Deniz, H.; Ernst, A.; Hazra, B. K.; Meyerheim, H. L.; Parkin, S. S. Thickness-Tunable Zoology of Magnetic Spin Textures Observed in Fe₅GeTe₂. *ACS Nano* **2024**, *18*, 5335–5343, PMID: 38315563.
- (10) Laref, S.; Kim, K.-W.; Manchon, A. Elusive Dzyaloshinskii-Moriya interaction in monolayer Fe₃GeTe₂. *Phys. Rev. B* **2020**, *102*, 060402.
- (11) Ly, T. T. et al. Direct Observation of Fe-Ge Ordering in Fe_{5-x}GeTe₂ Crystals and Resultant Helimagnetism. *Advanced Functional Materials* **2021**, *31*.
- (12) Silinskas, M.; Senz, S.; Gargiani, P.; Ruiz, A.; Kalkofen, B.; Kostanovski, I.; Mohseni, K.; Baldoví, J.; Meyerheim, H.; Parkin, S.; Bedoya-Pinto, A. Self-Intercalation as Origin of High-Temperature Ferromagnetism in Epitaxially Grown Fe₅GeTe₂ Thin Films. *Physical Review Letters* **2024**, *133*.
- (13) Chakraborty, A.; Srivastava, A. K.; Sharma, A. K.; Gopi, A. K.; Mohseni, K.; Ernst, A.; Deniz, H.; Hazra, B. K.; Das, S.; Sessi, P.; Kostanovskiy, I.; Ma, T.; Meyerheim, H. L.; Parkin, S. S. P. Magnetic Skyrmions in a Thickness Tunable 2D Ferromagnet from a Defect Driven Dzyaloshinskii-Moriya Interaction. *Advanced Materials* **2022**, *34*.
- (14) Belmeguenai, M.; Adam, J.-P.; Rousigné, Y.; Eimer, S.; Devolder, T.; Kim, J.-V.; Cherif, S. M.; Stashkevich, A.; Thiaville, A. Interfacial Dzyaloshinskii-Moriya interaction in perpendicularly magnetized Pt/Co/AlO_x ultrathin films measured by Brillouin light spectroscopy. *Physical Review B* **2015**, *91*.
- (15) Park, T.-E. et al. Néel-type skyrmions and their current-induced motion in van der Waals ferromagnet-based heterostructures. *Physical Review B* **2021**, *103*.
- (16) Cheynis, F.; Masseboeuf, A.; Fruchart, O.; Rougemaille, N.; Toussaint, J. C.; Belkhou, R.; Bayle-Guillemaud, P.; Marty, A. Controlled Switching of Néel Caps in Flux-Closure Magnetic Dots. *Physical Review Letters* **2009**, *102*.
- (17) Ribeiro, M.; Gentile, G.; Marty, A.; Dosenovic, D.; Okuno, H.; Vergnaud, C.; Jacquot, J.-F.; Jalabert, D.; Longo, D.; Ohresser, P.; Hallal, A.; Chshiev, M.; Boulle, O.; Bonell, F.; Jamet, M. Large-scale epitaxy of two-dimensional van der Waals room-temperature ferromagnet Fe₅GeTe₂. *npj 2D Materials and Applications* **2022**, *6*.
- (18) Ershadrad, S.; Ghosh, S.; Wang, D.; Kvashnin, Y.; Sanyal, B. Unusual Magnetic Features in Two-Dimensional Fe₅GeTe₂ Induced by Structural Reconstructions. *The Journal of Physical Chemistry Letters* **2022**, *13*, 4877–4883.
- (19) May, A. F.; Ovchinnikov, D.; Zheng, Q.; Hermann, R.; Calder, S.; Huang, B.; Fei, Z.; Liu, Y.; Xu, X.; McGuire, M. A. Ferromagnetism Near Room Temperature in the Cleavable van der Waals Crystal Fe₅GeTe₂. *ACS Nano* **2019**, *13*, 4436–4442.
- (20) Lv, X.; Pei, K.; Yang, C.; Qin, G.; Liu, M.; Zhang, J.; Che, R. Controllable Topological Magnetic Transformations in the Thickness-Tunable van der Waals Ferromagnet Fe₅GeTe₂. *ACS Nano* **2022**, *16*, 19319–19327.
- (21) Adhikari, A.; Mahato, B. K.; Sahoo, S.; Mukhopadhyay, S.; Palit, M.; Bera, S.; Datta, S.; Mondal, M.; Barman, A. Room Temperature Evolution of Laser-Induced Ultrafast Spin and Phonon Dynamics in 2D van der Waals Magnets Fe_xGeTe₂ (x = 3, 4, 5). *Advanced Functional Materials* **2024**,
- (22) Zhao, Y.; Song, Q.; Yang, S.-H.; Su, T.; Yuan, W.; Parkin, S. S. P.; Shi, J.; Han, W. Experimental Investigation of Temperature-Dependent Gilbert Damping in Permalloy Thin Films. *Scientific Reports* **2016**, *6*.

- (23) Gladii, O.; Haidar, M.; Henry, Y.; Kostylev, M.; Bailleul, M. Frequency nonreciprocity of surface spin wave in permalloy thin films. *Physical Review B* **2016**, *93*.
- (24) Sutter, E.; Komsa, H.-P.; Poretzky, A. A.; Unocic, R. R.; Sutter, P. Stacking Fault Induced Symmetry Breaking in van der Waals Nanowires. *ACS Nano* **2022**, *16*, 21199–21207.
- (25) May, A. F.; Bridges, C. A.; McGuire, M. A. Physical properties and thermal stability of Fe_{5-x}GeTe₂ single crystals. *Physical Review Materials* **2019**, *3*.
- (26) Li, D.; Haldar, S.; Kollwitz, L.; Schrautzer, H.; Goerzen, M. A.; Heinze, S. Prediction of stable nanoscale skyrmions in monolayer Fe₅GeTe₂. *Physical Review B* **2024**, *109*.
- (27) Ghosh, S.; Ershadrad, S.; Borisov, V.; Sanyal, B. Unraveling effects of electron correlation in two-dimensional Fe_nGeTe₂ (n = 3, 4, 5) by dynamical mean field theory. *npj Computational Materials* **2023**, *9:1* **2023**, *9*, 1–16.
- (28) Kalinikos, B. A.; Slavin, A. N. Theory of dipole-exchange spin wave spectrum for ferromagnetic films with mixed exchange boundary conditions. *Journal of Physics C: Solid State Physics* **1986**, *19*, 7013.
- (29) Balan, C.; van der Jagt, J. W.; Fassatoui, A.; Peña Garcia, J.; Jeudy, V.; Thiaville, A.; Bonfim, M.; Vogel, J.; Ranno, L.; Ravelosona, D.; Pizzini, S. Improving Néel Domain Walls Dynamics and Skyrmion Stability Using He Ion Irradiation. *Small* **2023**, *19*.